Friction **12**(7): 1434–1448 (2024)
https://doi.org/10.1007/s40544-023-0782-2
ISSN 2223-7690
CN 10-1237/TH
RESEARCH ARTICLE

Low friction under ultrahigh contact pressure enabled by self-assembled fluorinated azobenzene layers

Dandan XUE[1], Zhi XU[1], Linyuan GUO[1], Wendi LUO[2], Liran MA[1,*], Yu TIAN[1,*], Ming MA[1,*], Qingdao ZENG[2,*], Ke DENG[2], Wenjing ZHANG[1], Yichun XIA[1], Shizhu WEN[1], Jianbin LUO[1]

[1] *State Key Laboratory of Tribology in Advanced Equipment, Tsinghua University, Beijing 100084, China*

[2] *National Center for Nanoscience and Technology, Beijing 100190, China*

Received: 04 April 2023 / Revised: 11 May 2023 / Accepted: 19 May 2023

Abstract: Extensive efforts have been made to pursue a low-friction state with promising applications in many fields, such as mechanical and biomedical engineering. Among which, the load capacity of the low-friction state has been considered to be crucial for industrial applications. Here, we report a low friction under ultrahigh contact pressure by building a novel self-assembled fluorinated azobenzene layer on an atomically smooth highly-oriented pyrolytic graphite (HOPG) surface. Sliding friction coefficients could be as low as 0.0005 or even lower under a contact pressure of up to 4 GPa. It demonstrates that the low friction under ultrahigh contact pressure is attributed to molecular fluorination. The fluorination leads to effective and robust lubrication between the tip and the self-assembled layer and enhances tighter rigidity which can reduce the stress concentration in the substrate, which was verified by density functional theory (DFT) and molecular dynamics (MD) simulation. This work provides a new approach to avoid the failure of ultralow friction coefficient under relatively high contact pressure, which has promising potential application value in the future.

Keywords: ultrahigh contact pressure; self-assembled layer; fluorination; robust lubrication

1 Introduction

Reducing friction is a crucial method for energy dissipation reduction in mechanical sliding systems, which has become increasingly significant for energy savings and life extension of mechanical components [1–5]. Superlubricity is a typical low friction state where friction nearly vanishes [6]. In the 1990s, Hirano and Shinjo [7], and Sokoloff [8] theoretically predicted the existence of superlubricity by carefully considering the detailed phenomena at the atomic scale, in which the sliding interfaces have characteristics such as atomic flatness, rigidity, structural incommensurability (i.e., non-matching), molecular cleanliness, and weak interaction. A prominent strategy to achieve superlubricity under a certain load-bearing capacity has attracted increasing interest [9, 10]. Hitherto, few superlubricity studies under contact pressures higher than 1 GPa have been reported [11–13]. At macroscales, liquid superlubricity under an ultrahigh contact pressure of 1.19 GPa was realized by lubrication with partially-oxidized black phosphorus (PoBP) nanosheets, owing to the abundant P=O and P–OH bonds formed on the nanosheet surfaces [11]. At the microscale, superlubricity with a high contact pressure of up to 1 GPa was achieved between a graphene-coated silica (SiO_2) microsphere and graphene on hexagonal boron nitride surfaces [12], and a contact pressure of 2.52 GPa was achieved by sliding graphene-nanoflakes transferred onto a silicon tip against graphite due to incommensurate contact [13]. Inspired by these results, the load-bearing capacity of superlubricity still needs

* Corresponding authors: Liran MA, E-mail: maliran@tsinghua.edu.cn; Yu TIAN, E-mail: tianyu@tsinghua.edu.cn; Ming MA, E-mail: maming16@tsinghua.edu.cn; Qingdao ZENG, E-mail: zengqd@nanoctr.cn

to be improved to achieve practical utilizations. In order to achieve superlubricity under higher contact pressure, it is necessary to find the synergistic effect of low friction materials and regulation of sliding layers that can prevent notable deformations and energy dissipation in the contact area.

Low friction can be realized by self-assembled molecular layers due to their strong bonding with the substrate, low surface energy, and high stability [14–16]. For instance, microscale solid superlubricity can be accomplished by uniform ordered self-assembly of several liquid crystals [17] or by attaching sodium dodecylsulfate (SDS) molecular layers on friction surfaces [18]. Fluorinated self-assembled molecular layers can significantly enhance the load-bearing capacity by 1.5 times (from 12.4 to 18.2 MPa) in the superlubricity state by enhancing the interaction between water and the self-assembled layer, which results in a more robust layered water structure confined in the contact zone [19]. Fluorinated self-assembled molecular layers have low surface energy and outstanding stability due to their high electronegativity, lone-pair electrons [20], and significant interaction with the π-electron system in the aromatic ring [21]. In addition, self-assembled materials exhibit strongly influence the friction properties [22–24]. Azobenzene, widely used in forming self-assembled layers, can be easily modified to realize unique structural characteristics by attaching different multifunctional substituents to the parent molecules [25–27], such as self-assembled azobenzene molecule surfaces for self-oscillating/self-cleaning [28] and the self-assembled azobenzene polymer network coating of a robot finger for controlling the friction coefficient [29]. In particular, fluorination may alter the electronic spectra and several physical parameters of azobenzene [30], and also improve its stability [31]. Moreover, the rigidity and surface energy of the self-assembled molecular layers will be changed after modification. Overall, the use of the fluorinated azobenzene self-assembled layer can be an effective synergistic strategy to realize low friction under higher contact pressure, by considerably enhancing the rigidity of the self-assembled layer and effectively preventing energy dissipation through sliding [32].

This work proposed a stable low friction state under an ultrahigh contact pressure of 4.11 GPa by building a novel self-assembled fluorinated azobenzene layer on an atomically smooth highly-oriented pyrolytic graphite (HOPG) surface. The friction properties of the fluorinated azobenzene self-assembled layer compared with the non-fluorinated layer were measured using atomic force microscopy (AFM). The mechanism of low friction under high contact pressure was revealed through theoretical simulations.

2 Experimental

2.1 Materials

The reaction solvents used in the experiments were purchased from J&K Chemical Ltd. (Beijing, China), and were used without any further purification. All other solvents and chemicals, including ethanol and acetone et al., were supplied by Aladdin. The HOPG with a mosaic spread of 0.4° (grade ZYA) was purchased from Advanced Ceramics Inc. in Cleveland USA. A freshly cleaved graphite surface was obtained by mechanically exfoliating the HOPG.

2.2 Synthesis of compounds

The (E)-4,4'-(diazene-1,2-diyl)bis(2-fluorobenzoic acid) (*tran*-NN2A-F) and (E)-4,4'-(diazene-1,2-diyl)dibenzoic acid (*tran*-NN2A) compounds were synthesized according to a reported procedure [33]. In the synthesis procedure, NN2A-F was obtained in the yield of 65 wt% and then treated with ultraviolet light to obtain *cis*-NN2A-F (see Fig. 1(a)). The time of UV light irradiation with 360 nm is 40 min and the power is 8 W/m. The ^{1}H nuclear magnetic resonance spectra (^{1}H NMR) data of *cis*-NN2A-F were obtained to determine the molecular structure, as shown in Fig. 1(c), and microscopic granular particles were observed by scanning electron microscopy (SEM) (see Fig. 1(d)). The synthesis and characterization of *cis*-NN2A were similar to those of *cis*-NN2A-F (see Figs. 1(b), 1(e), and 1(f)). The details are described below.

The synthesis procedures of the two azobenzene compounds are presented in Figs. 1(a) and 1(b). The ortho-fluorine *p*-Nitrobenzoic acid (8.0 mmol) was mixed with NaOH (90.0 mmol) in distilled water (80.0 mL), and stirred until the substances were dissolved completely. Then glucose (45.0 mmol) was

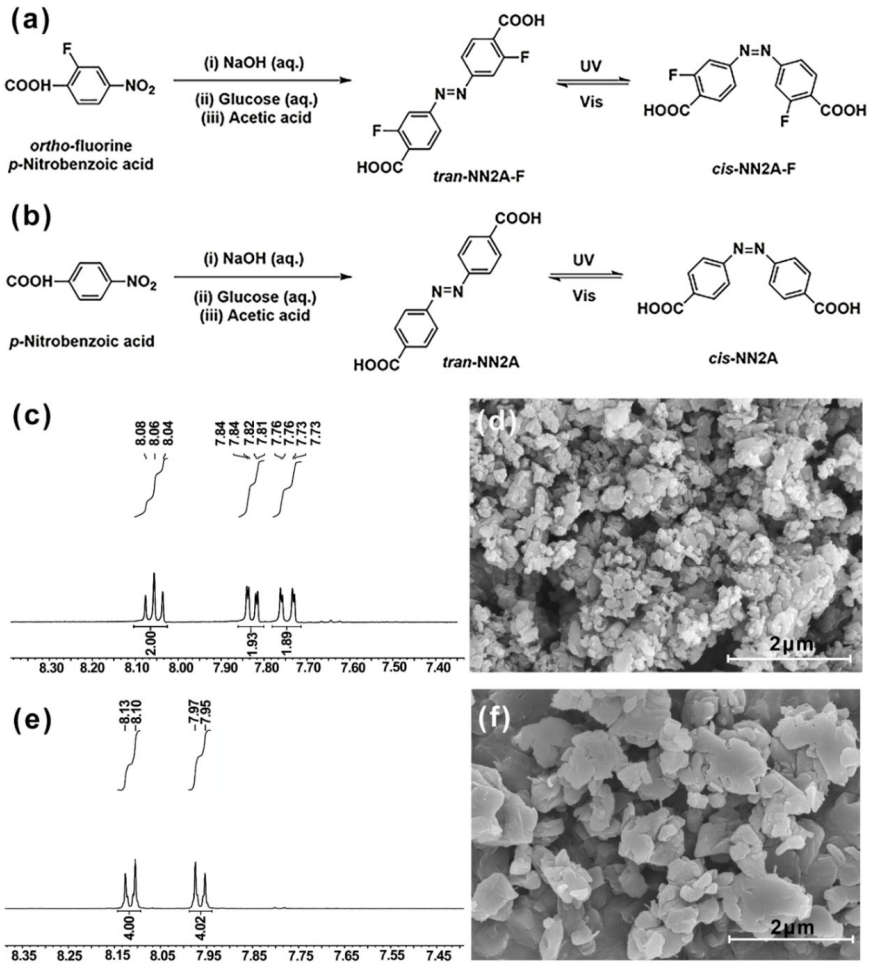

Fig. 1 Synthesis and characterization of two azobenzene carboxylic acids. (a) Synthesis procedure of *cis*-NN2A-F; (b) synthesis procedure of *cis*-NN2A; (c) ^{1}H NMR data of *cis*-NN2A-F; (d) SEM image of *cis*-NN2A-F particles; (e) ^{1}H NMR data of *cis*-NN2A; and (f) SEM image of *cis*-NN2A particles.

dropwise added into the orange–yellow *p*-Nitrobenzoic solution at 80 °C, and reacted for 8 h in the atmosphere. After centrifugation, the brown product in the aqueous solution was acidified with acetic acid (20.0 mL), and then final centrifuged with distilled water. The (E)-4,4'-(diazene-1,2-diyl)bis(2-fluorobenzoic acid) (2.6 mmol, 65%) abbreviated *tran*-NN2A-F was obtained. The compound was treated with ultraviolet light to obtain *cis*-NN2A-F. The time of UV light irradiation with 360 nm is 40 min and the power is 8 W/m. The ^{1}H NMR data of *cis*-NN2A-F were obtained to determine the molecular structure, as shown in Fig. 1(c), and granular particles were observed by SEM (shown in Fig. 1(d)). ^{1}H NMR (600 MHz, $CDCl_3$): δ 8.08–8.04 (t, 2H), 7.84–7.81 (dd, 2H), 7.76–7.73 (dd, 2H). EA calcd for $C_{14}H_8F_2N_2O_4$ (306.22 g·mol^{-1}): C 54.91%, H 2.63%, F 12.41%, N 9.15%, O 20.90%; Found: C 54.82%, H 2.60%, F 12.32%, N 9.11%, O 20.81%. Similar to the *cis*-NN2A compound, the synthon of *cis*-NN2A is p-Nitrobenzoic acid with 72 wt% synthetic yield. ^{1}H NMR data of *cis*-NN2A were detected to determine the molecular structure (as Fig. 1(e)) and lamellar particles were observed though SEM (shown in Fig. 1(f)). The results showed that the two compounds have been successfully synthesized bearing different distinct morphologies. ^{1}H NMR (600 MHz, $CDCl_3$): δ 8.12 (d, 4H), 7.96 (d, 4H). EA calcd for $C_{14}H_{10}N_2O_4$ (270.24 g·mol^{-1}): C 62.22%, H 3.73%, N 10.37%, O 23.68%; Found: C 62.17%, H 3.70%, N 10.30%, O 23.29%.

2.3 Preparation of self-assembled molecular layers

HOPG substrates were prepared with a size of 0.5 cm × 0.5 cm. Both *cis*-NN2A and *cis*-NN2A-F were separately

dissolved in heptanoic acid (HA) by sonication at concentrations less than 1.0×10^{-4} M, and then a droplet of *cis*-NN2A or *cis*-NN2A-F solution (0.5 μL) was deposited onto a newly peeled atomically flat HOPG substrate by pipette, generating the self-assembled layer samples. The solution lying flat on the HOPG substrate was placed motionlessly in a clean environment to yield the target self-assembled layer. This layer grew as the solution spread out on the HOPG substrate without depending on external forces. Upon completion of the self-assembly process, the prepared molecular layer samples were quiescent at room temperature prior to testing.

2.4 Characterization of self-assembled molecular layers

2.4.1 Scanning tunneling microscopy (STM) investigation

STM characterization experiments were carried out at solid/liquid interfaces after immersing the tip into the solution using a NanoScope IIIa instrument (Bruker, USA) in an atmospheric environment. The STM tips were obtained by mechanically cutting Pt/Ir (80/20) wires to atomic sharpness. The STM images were recorded using the cut tip in constant-current mode. The images were presented as raw data without further modification. The drift for all the images was calibrated using an atomic-resolution HOPG lattice as a reference. The cell parameter data were measured by the length measurement function of the STM software "NanoScope (R) III Digital Instrument" (Veeco Instrument Inc. America). All of the data were averaged to determine the final cell parameters.

2.4.2 AFM force measurements

Lateral forces (friction) of the self-assembled samples were measured by MFP-3D AFM (Asylum Research, USA) with a multi-tip probe (HQ: XSC11, nominal normal spring constant of 2.7 N/m) at room temperature. To eliminate the effect of the solvent, sample measurements were conducted at the gas–solid sample interface after the solvent evaporated. It is of vital important that the genuine normal force and lateral factors need to be calibrated prior to measurements. Primarily, the sensitivity of the normal photodetector was calculated from the slope of the force curve acquired on a hard substrate. Then, the power spectral density of thermal noise fluctuations under environmental conditions can be used to estimate the normal spring constant [34]. Then, the voltage result was transformed into force values, and the lateral factor was calculated based on the improved wedge calibration method by scanning the commercial TGF11 silicon grating (MikroMasch, Estonia) [35]. The AFM force tests were scanning in the direction perpendicular to the cantilever in contact mode with a 1 Hz scan rate and a scan size of 100 nm × 100 nm, which was similar to the STM characterization conditions. In addition, to ensure the noise of the deflection signal, the feedback gains should be adjusted to appropriate levels during the measurements. Similarly, the friction values were calculated as half of the difference between the trace and retrace signals in order to exclude the topography effect. A schematic diagram of the AFM measurement process is shown in Fig. 2(a).

2.5 Density functional theory (DFT) calculations

Theoretical calculations were performed using the DFT-D scheme implemented in the DMol3 code [36]. To describe the 2D periodic structure on graphite, periodic boundary conditions (PBCs) were chosen. The Perdew–Burke–Ernzerh parameterization of the local exchange correlation energy was applied in the generalized gradient approximation (GGA) to describe the exchange and correlation [37]. Grimme's dispersion theory was also applied to correct the dispersion interactions of van der Waals (vdW) interactions. All electron spin-unrestricted Kohn–Sham wave functions were expanded in a local atomic orbital basis. For the large system, the numerical basis set was applied. All calculations were all electron calculations and were performed with a medium mesh. A self-consistent field procedure was performed with a convergence criterion of 10^{-5} au for the energy and electron density. To evaluate the interactions between the HOPG and the adsorbates, a model system was established. Since the adsorption of benzene on graphite and graphene should be very similar [38], the calculations were performed on infinite graphene monolayers using PBCs. Considering that the interaction between adsorbates and substrate was mainly van der Waals interactions, Grimme's dispersion corrections were

adopted in the calculations. In the superlattice, slabs were separated by 35 Å in the normal direction. When modeling the adsorbates on graphene, the graphene supercells were used and sampled the Brillouin zone by a 1×1×1 *k*-point mesh.

2.6 Molecular dynamics (MD) simulations

In this Section, the details of the MD simulations for two systems were given: (1) AFM tip sliding on graphene with non-fluorinated layer and (2) AFM tip sliding on graphene with fluorinated layer.

2.6.1 Simulation system

The intralayer interactions of graphene sheets were modeled using the Tersoff force field [39], which is widely used for graphene. The interlayer interactions for carbon atoms belonging to the different graphene layers were modeled using the Lennard–Jones potential with the two parameters c =2.84 meV and σ_c =0.34 nm [40]. The silicon tip was modeled using the Lennard–Jones potential with the two parameters Si =0.0279 eV and σ_{Si} =0.25 nm [40]. The *cis*-NN2A or *cis*-NN2A-F molecules were modeled using OPLS-AA force field [41]. Lorentz–Berthelot mixing rules were used for the intermolecular van der Waals (vdW) interactions. Truncated and force-shifted Lennard–Jones interaction that combines the standard Lennard–Jones function and subtracts a linear term based on the cutoff distance was used here [42], so that both, the potential and the force, go continuously to zero at the cutoff of 1.2 nm. All MD simulations were carried out using a time step of 1 fs.

2.6.2 Simulation procedure

The two systems had the same simulation procedure, which includes the following steps: Equilibrating the system, starting dragging, and collecting data.

Equilibrating the system. The normal force was applied on the silicon tip to generate a pressure comparable with the experiments. The bottom graphene layer was fixed. A temperature of 298 K was maintained by applying the Nose–Hoover chain thermostat to the self-assembling molecules and the top graphene layer. The equilibration lasted for 100 ps.

Starting dragging and collecting data. A temperature of 298 K was maintained by applying the Langevin thermostat to the top graphene layer only [43], so that the heat produced by the slip and viscous friction in the system was removed through the graphene, as is done in a real experiment. The tip was dragged by an imaginary body with a constant velocity (v = 10 m/s) along the y-axis. The stiffness between the tip and the imaginary body was 10 N/m. The friction force was recorded during the dragging process of 5 ns.

3 Results and discussion

3.1 Self-assembled layer structures

The self-assembly of the fluorinated layer (*cis*-NN2A-F layer) and non-fluorinated layer (*cis*-NN2A layer) were prepared (see Methods) as the schematic illustration (see Figs. 2(a)–2(d)). In our previous research, we demonstrated the NN2A self-assembled structures [44]. After the self-assembled layers were fabricated, the chemical composition on the surfaces were detected via X-ray photoelectron spectroscopy (XPS). The C 1s profiles of non-fluorinated layer (see Fig. S1 in the Electronic Supplementary Material (ESM)) and fluorinated layer (see Fig. 2(e)) were clearly contrasted. The absorption peaks were assigned to the C–C, C–N, and C=O bonds [45]. The binding energies of the corresponding bonds in the fluorinated layer were shifted to the right and the appearance of a new peak in the spectrum indicated a C–F bond [46]. In addition, the obvious peaks of the F–F bond and F–C bonds were observed in the F 1s profile of the fluorinated layer (see Fig. 2(f)) [47]. These results suggested that the *cis*-NN2A-F molecules were successfully self-assembled on the HOPG substrate.

To investigate the morphology of the self-assembled molecular layer, STM was performed. The STM image revealed that the self-assembled layers had a pronounced layered structure, and the detailed processes of growth and measurement are described in Section 2. High-resolution STM characterization images and corresponding molecular models of the non-fluorinated layer were shown in Figs. 2(g) and 2(h), and those of the fluorinated layer were shown in Figs. 2(i) and 2(j). The structural differences of the self-assembled molecular layers were caused by molecular fluorination. It was observed that both self-assembled molecules were closely connected. The

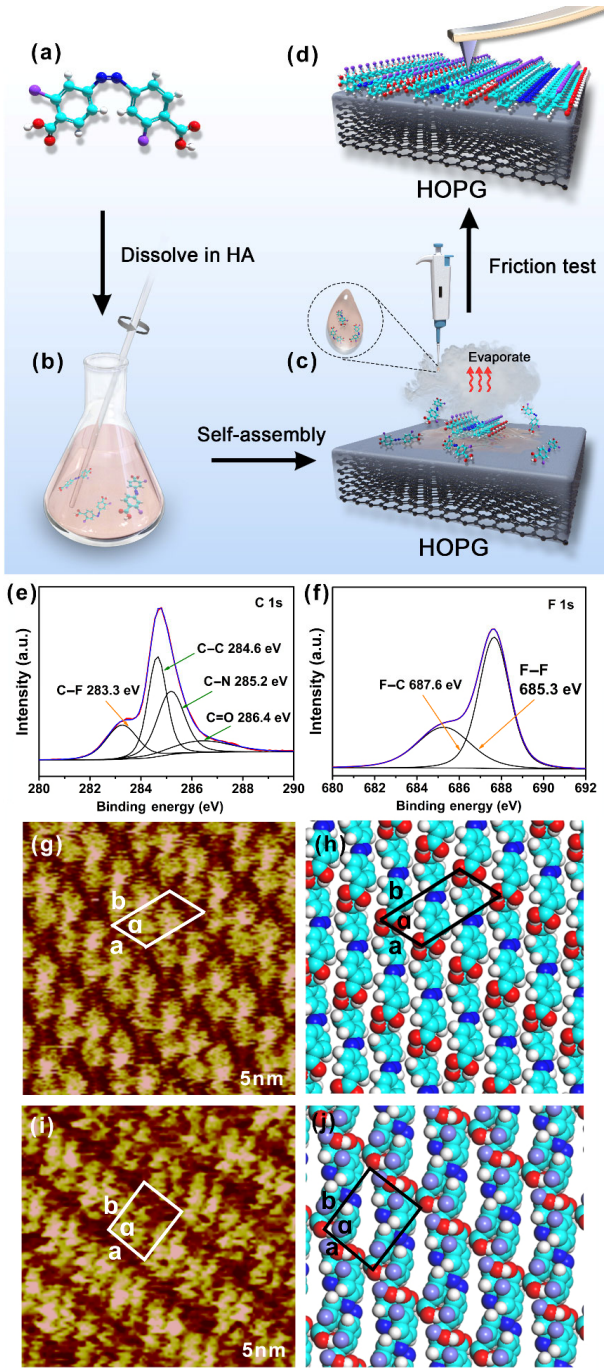

Fig. 2 Schematic fabrication process and characterizations of the self-assembled layers. (a)–(d) Schematic fabrication process of self-assembled layer. XPS characterization: (e) C 1s spectrum of the fluorinated layer and (f) F 1s spectrum of the fluorinated layer. (g) High-resolution STM image of non-fluorinated quadrilateral structures (V_{bias}=688.9 mV and I_{set}=299.8 pA) and (h) corresponding molecular model of the non-fluorinated layer structures; (i) high-resolution STM image of fluorinated quadrilateral structures (V_{bias}=688.9 mV and I_{set}=299.8 pA); and (j) corresponding molecular model of the fluorinated layer structures.

unit cells of the non-fluorinated layer were marked by boxes in Figs. 2(g) and 2(h). The width of the unit cell was a = 0.56±0.1 nm and the length was measured as b = 1.17±0.1 nm, with an inclination angle of α = 65°±1°. The unit cell parameters containing one *cis*-NN2A molecule are listed in Table 1. Hydrogen bonds formed by the adjacent *cis*-NN2A carboxylic acid groups were arranged in parallel between the bright molecules. The two bright spots in each *cis*-NN2A correspond to the two benzene units in the molecules. The molecular arrangement was stable due to the van der Waals forces and hydrogen-bond interactions, which forces between the self-assembled molecules and the HOPG substrate, as well interactions between the molecules.

For the fluorinated layer, the self-assembled arrangement mechanism was verified. STM was utilized to study the morphology of the fluorinated layer on the heptanoic acid (HA)/HOPG interface (see Figs. 2(i) and 2(j)). Some obvious changes in the self-assembled structure were found by analyzing the STM images. Regarding the arrangement of the self-assembled molecular layer, the fluorine atoms were all arrayed on the same side. The fluorinated *cis*-NN2A-F were vertically arranged and the intermolecular gap between the two molecules led to a smaller width of the unit cell. Moreover, the length of the unit cell decreased with the degree of fold increased during the connection of molecules. The unit cell parameters containing two *cis*-NN2A-F molecules marked on the STM image in fluorinated layer were measured as follows: a = 0.83±0.1 nm, b = 1.04±0.1 nm, and α = 91°±1°. All of the unit cell parameters are summarized in Table 1.

3.2 Frictional characteristics

Before prior to each AFM measurement, the self-assembled layer structures were studied by STM to observe the arrangement of the molecules. The friction

Table 1 Experimental (expt.) and calculated (cal.) unit cell parameters of the non-fluorinated and fluorinated layers on the HOPG surface. The measurement error for the length was 0.1 nm, and that of the angle was 1°.

System		a (nm)	b (nm)	α (°)
Non-fluorinated layer	Cal.	0.56	1.17	65
	Expt.	0.56±0.1	1.17±0.1	65±1
Fluorinated layer	Cal.	0.83	1.04	91
	Expt.	0.83±0.1	1.04±0.1	91±1

properties of the self-assembled molecular layers were measured to investigate the effect of fluorination, using MFP-3D AFM (lateral force mode) under ambient conditions. With a silicon probe sliding on the surface of the self-assembled molecular layer based on the HOPG substrate (see Fig. 2(d)), lateral forces (friction) were measured by the half width of the lateral force loop under different applied loads, and the measurement process was described in detail in Section 2.

For frictional experiments, the friction forces of the non-fluorinated layer, fluorinated layer, and HOPG as a function of the applied load are presented (see Fig. 3(a)). The friction forces increased linearly with increasing load for all of the friction systems. The friction–load data were linearly fitted to obtain the friction coefficient (μ), which can be defined as the slope of the linear fitting curve (labeled in Fig. 3(a)). Interestingly, the friction coefficient of the fluorinated layer was the lowest among the three systems. For the non-fluorinated layer, the friction coefficient of friction was approximately 0.01. By contrast, the friction coefficient of the fluorinated layer reached 0.0005, corresponding to a low friction state. That is, the friction coefficient of the fluorinated layer was reduced by approximately one order of magnitude, indicating that the fluorinated layer possessed much better lubrication properties.

Generally speaking, at the nanoscale, the frictional forces can be represented by Eq. (1), which has been mentioned above in the calculation of friction coefficients. The average friction forces of both self-assembled layers increased linearly with increasing normal load, ensuring accurate calculation of the friction coefficient.

$$F_s = \mu F_n + F_0 \tag{1}$$

where F_s represents the frictional force, F_n refers to the normal load, and μ is defined as the friction coefficient according to the slope of the friction versus normal load curve, which was equal to $(F_s–F_0)/F_n$. In addition, F_0 is the offset friction when the applied load is 0 and proportionated to the adhesive force. Herein, F_0 of the non-fluorinated layer is 4.3 nN, and F_0 of the fluorinated layer is 4.6 nN (see Fig. 3(a)).

Typical friction loops under an applied load of 400 nN (F_n) in the fluorinated layer can achieve a

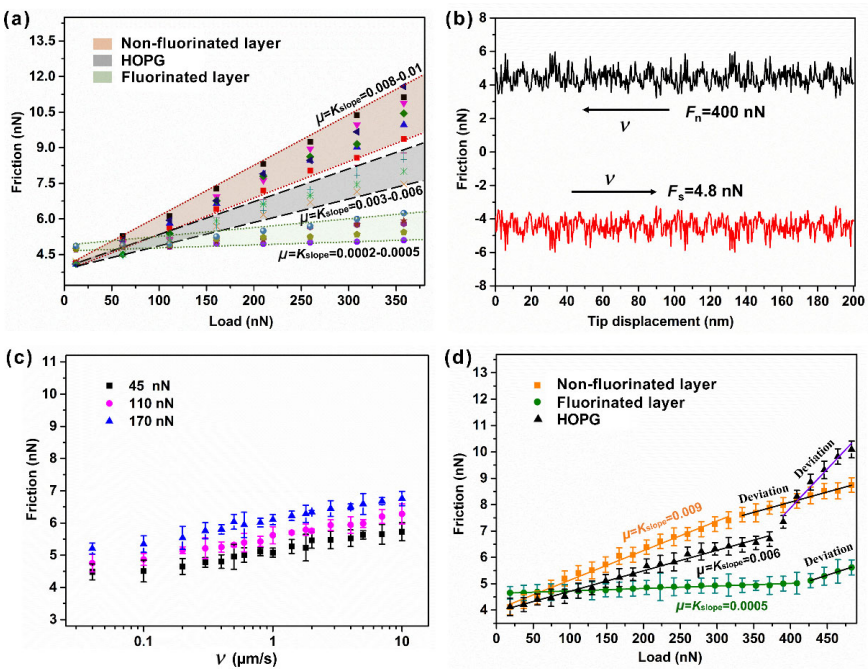

Fig. 3 Friction properties. (a) Lateral force (friction) as a function of the applied load for different self-assembled layers or HOPG; (b) typical frictional force loop under a constant load of 400 nN in the fluorinated layer; (c) friction of the fluorinated layer under different sliding speeds (0.04–10 μm/s) under the loads of 45, 110, and 170 nN; and (d) maximal applied load, with the deviation of the frictional force from the baseline.

friction force of F_s = 4.8 nN (see Fig. 3(b)). Then the μ was calculated as 0.0005, and the friction experiments had been repeated more than 20 times. It was confirmed that the fluorinated layer can reach a low friction state. In order to explore the influence of different sliding speeds on the friction coefficient, a series of experiments were designed. The basic friction forces were obtained under several speeds (see Fig. 3(c)) at three different loads. The friction coefficients (slope of fitting lines) were almost identical, while the friction forces increased. This is most likely due to the adhesion between the molecules and the tip that was enhanced at higher sliding speed. Therefore, sliding speeds had a remarkable effect on the friction behavior under a certain range of speeds.

To further study insight into the load-bearing capacity at the low friction state of the fluorinated layer, we carried out a series of tests in which the normal load increased continuously until the friction forces began to increase sharply (see Fig. 3(d)). It was observed that the friction of the fluorinated layer deviated at approximately 420 nN. While for the non-fluorinated layer and HOPG, the friction deviated significantly when the normal load reached 350 and 330 nN, respectively. According to Hertz contact theory, the maximum contact pressure of the fluorinated layer was calculated as 4.11 GPa, while it was 3.16 GPa for the non-fluorinated layer and 1.81 GPa for HOPG. It can be clearly observed that the fluorinated layer can withstand a much higher load-bearing capacity than the non-fluorinated layer, so the importance of fluorination was witnessed in the load-bearing capacity. SEM characterization of the AFM tip in the measured process was conducted to determine the tip radius of the contact zone, which was 35 nm (see Fig. S3 in the ESM). In addition, we recalibrated the elastic modulus of the coupling system including the self-assembled molecules and the HOPG substrate using a diamond probe. Then, Abaqus simulations results showed the maximum Hertz contact pressure under the maximal applied load was 5.97 GPa (see Fig. S4 in the ESM), indicating that the fluorinated layer had the maximum Hertz contact pressure corresponding to the results of the experiment.

In another series of experiments, the interactions between the probe and the two self-assembled layers were investigated, and the probe continuously approached the self-assembled layer surfaces and then retracted (see Figs. 4(a) and 4(b)). The existence of adhesive forces between the probe and the self-assembled layer was indicated. Experimentally, the statistically pulled-out normal adhesive force was obtained as 16.9 nN when the probe started to be pulled out of contact from the non-fluorinated layer, which was fitted by a Gaussian distribution according to the 64 normal force curves (see Fig. 4(c)). Similarly, the adhesive force between the probe and the fluorinated layer was calculated as 22.8 nN based on the 64 normal force curves (see Fig. 4(d)). The results indicated that the probe against the fluorinated layer could be pulled out of contact with a higher normal load. The adhesive force of the fluorinated layer was 1.3-fold larger than that on the non-fluorinated layer, in agreement with the calculated load-bearing capacity values. This result also suggests that the fluorinated layer sustained a higher contact pressure.

3.3 Mechanism discussion

To explain our findings, we explored the low friction mechanism under ultrahigh contact pressure of the fluorinated layer using DFT calculations. DFT results demonstrated that the fluorinated *cis*-NN2A-F are vertically arranged, resulting in different binding sites and tighter ordering for the mean molecular spacing obtained for the unit cell parameters (Table 1). The adsorption energy between the silicon probe and the self-assembled layer was evaluated and found to be positively correlated with the static lateral force before the friction experiment (i.e., the intercept in the friction–load relationship). Figure 5 showed the molecular structure morphology of two self-assembled molecules in contact with silicon atoms. We set up simulation models for maximum correspondence with the conditions in the experiment. The models were established corresponding to two different molecular numbers with the same volume of silicon atom as well the interval distance. Initially, the atoms in the horizontal plane of the *cis*-NN2A molecules (see Figs. 5(a) and 5(c)) were contacted during the silicon tip sliding, while the *cis*-NN2A-F molecules (as Figs. 5(b) and 5(d)) made the most contact with the fluorine atoms in the longitudinal plane. The results showed that the adsorption energy per unit area between silicon atoms and *cis*-NN2A-F molecules was corresponded

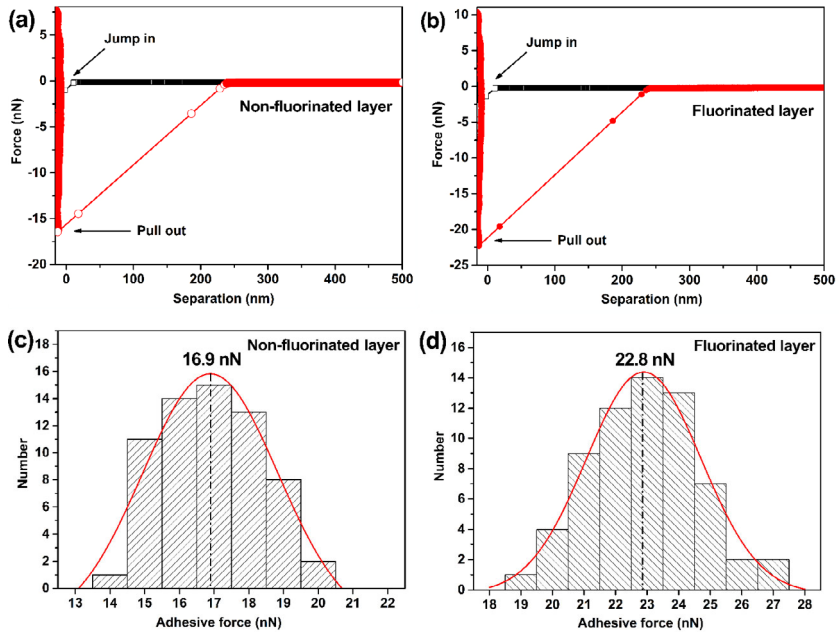

Fig. 4 Typical normal forces as functions of separations measured during the approaching and retracing processes. (a) Forces between the AFM probe and non-fluorinated layer; (b) forces between the AFM probe and fluorinated layer. Histogram of the adhesive force extracted from 64 normal force curves in an area of 500 nm × 500 nm: (c) Fitting the normal distribution of forces between the AFM probe and non-fluorinated layer gives an adhesive force of approximately 16.9 nN; (d) fitting the normal distribution of forces between the AFM probe and fluorinated layer gives an adhesive force of approximately 22.8 nN.

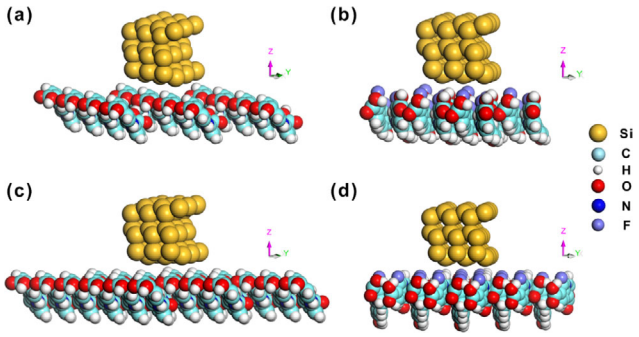

Fig. 5 Schematic diagram of DFT calculation of intermolecular adsorption energy between silicon atoms and different systems. (a) System consisting of the 12 *cis*-NN2A molecules; (b) system consisting of the 12 *cis*-NN2A-F molecules; (c) system consisting of the 18 *cis*-NN2A molecules; and (d) system consisting of the 18 *cis*-NN2A-F molecules.

to greater than that between silicon atoms and *cis*-NN2A molecules (Table 2). This finding was in agreement with the adhesive force relationship of the self-assembled layers obtained in the experiment. For the fluorinated layer, the greater adsorption energy per unit area contributed to easily carrying the molecules onto the tip, which was conducive to lubrication reducing the friction force. The importance of the molecular structure rearrangement was clearly witnessed, serving as supporting the above explanation of the low-friction mechanism under ultrahigh contact pressure.

To support our explanation, the experimental system was modeled in MD simulations (see Fig. 6(a)). The AFM tip was modeled as a silicon hemisphere to match the experiments. The diameter of the tip was approximately 5 nm, and the square double graphene layers had a side length of 8 nm. The number density of the self-assembled *cis*-NN2A and *cis*-NN2A-F was 1.6 nm^{-2}. In the simulations, periodic boundary conditions were applied along the three directions. The vacuum space in z direction was set as 2.6 nm, which is longer enough to avoid the ghost atom interference. The bottom graphene layer was fixed, and the normal force was applied on the atoms of the silicon tip. The tip was dragged with a constant velocity (v = 10 m/s) along the y-axis. All simulations were performed using LAMMPS [48] with a timestep of 1 fs. Although the radius of the silicon tip studied in the simulation (~5 nm) is slightly different from that in the experiments (~30 nm), the range of loading pressure is comparable, i.e., 0.55–3.74 GPa in both experiments and 0.001–1.57 GPa in simulations. As

Table 2 DFT calculation results of adsorption energies between self-assembled molecular layers and silicon atoms.

	Total adsorption energy (kcal·mol^{-1})	Area (Å^2)	Adsorption energy per unit area (kcal·mol^{-1}·Å^{-2})	Adsorption energy per unit area (eV·nm^{-2})
cis-NN2A (12)	–292.262	712.5754	–0.41015	–1.77857
cis-NN2A-F (12)	–270.783	517.8411	–0.52291	–2.26755
cis-NN2A (18)	–418.284	1068.863	–0.39134	–1.69701
cis-NN2A-F (18)	–354.367	776.7617	–0.45621	–1.97831

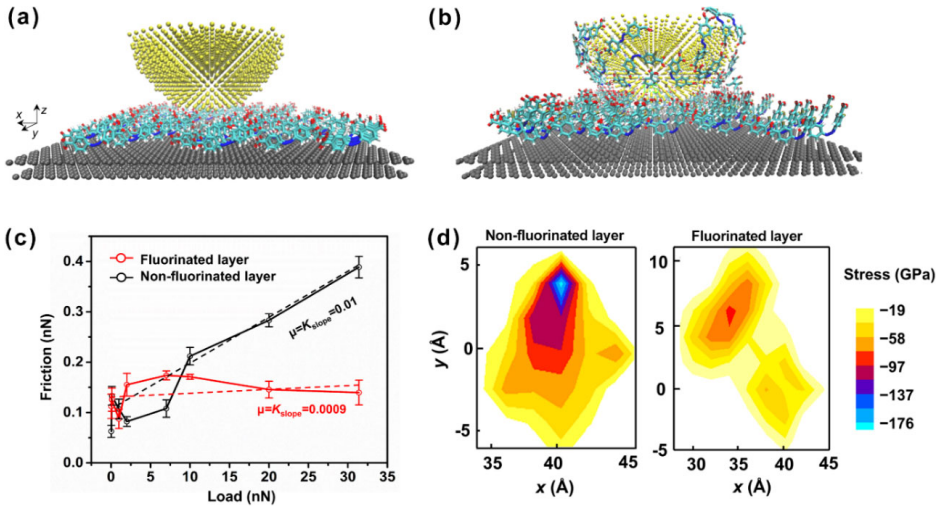

Fig. 6 MD simulations of AFM tip sliding on graphene with self-assembled molecular layers. (a) Atomistic model in the friction simulations. From top to bottom: the silicon tip (brown–yellow hemisphere), self-assembled molecules (*cis*-NN2A-F or *cis*-NN2A) and two graphene layers (gray layer); (b) side view of the schematic diagram showing different state distributions of the fluorinated layer upon the sliding process; (c) relationship between frictional force and load during sliding. The friction coefficients of the silicon tip sliding on the self-assembled fluorinated and non-fluorinated layers were 0.0009 and 0.01, respectively; and (d) distribution of the normal force (*z* direction) felt by the bottom graphene layer at the position of the silicon tip in the *x*-*y* plane for two systems with the same load of 1.57 GPa.

shown in Fig. 6(c), the friction coefficients ($\mu = K_{\text{slope}}$) for sliding on self-assembled non-fluorinated and fluorinated layers were different, which is 0.01 and 0.0009, respectively. These results were comparable with the values obtained in our experimental measurements (0.008–0.01 for non-fluorinated layer and 0.0002–0.0005 for fluorinated layer).

From the atomic snapshot during silicon tip sliding (as Videos in the ESM), it was found that silicon hemispheres were partially coated by both types of self-assembled molecules. A distribution state of the self-assembled molecules in the probe sliding process was shown in Fig. 6(b). The fluorinated molecules have a tighter rigidity coating, resulting in a smaller area where the silicon tip was directly in contact with the graphene layer. Quantitatively, the distribution of the normal force felt by the bottom graphene was calculated as shown in Fig. 6(d). The tighter rigidity coating of *cis*-NN2A-F molecules reduced the stress concentration in the HOPG substrate, demonstrating the mechanism for achieving low friction under the higher contact pressure of the fluorinated layer.

The position of the shear plane was important for revealing the underlying mechanism that gives rise to an ultralow friction coefficient. To determine the exact position of the shear plane, we carried out atomic phase experiments. The shear plane transformations of two layers were shown in Figs. 7(a)–7(d). For the non-fluorinated layer, we measured the atomic phase under a smaller load, while for the fluorinated layer, we measured the atomic phase under a larger load near the inflection point (see Fig. 7(e)). The position of shear plane was between the tip carrying molecules and the graphite layer. Then, load was applied exceeding the maximum to give out that the tip slides the graphite layer. The greater adsorption energy per unit area of the fluorinated layer contributed to easily carrying the molecules onto the tip to slide. By

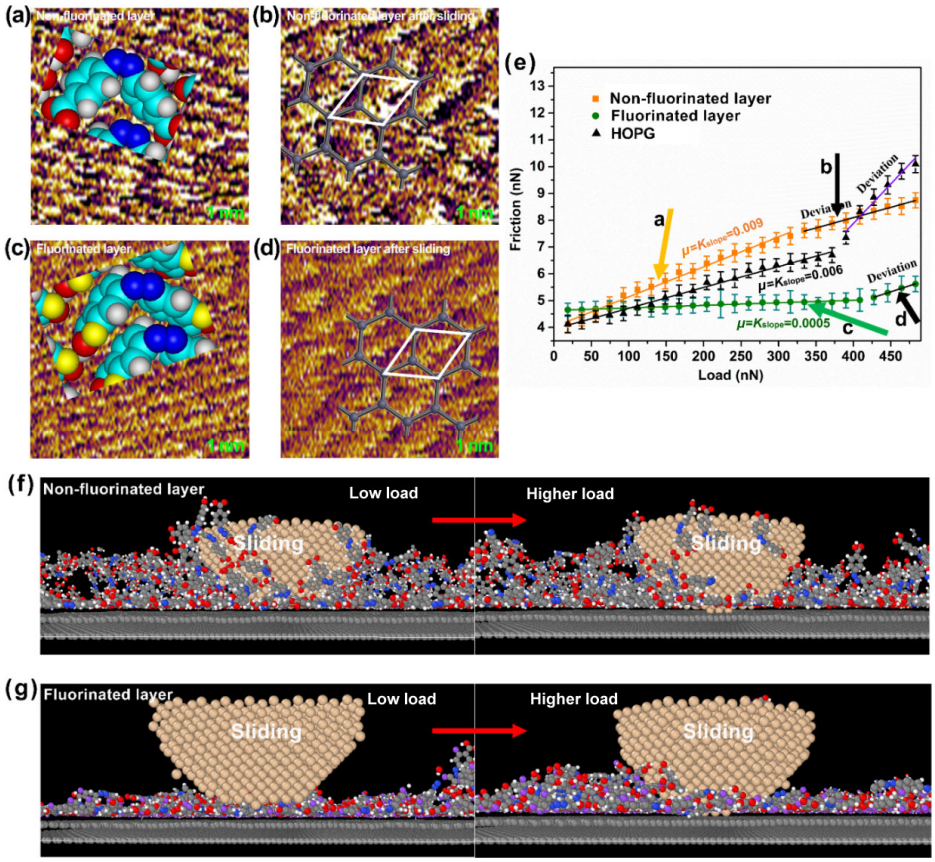

Fig. 7 Lattices of two molecular layers and that after frictional tests, and side views during sliding. (a) Atomic phase of non-fluorinated layer; (b) atomic phase of non-fluorinated layer after sliding; (c) atomic phase of fluorinated layer; (d) atomic phase of fluorinated layer after sliding; (e) tested loads of atomic phase corresponding to the friction image; (f) shear planes under different loads of non-fluorinated layer; and (g) shear planes under different loads of fluorinated layer.

comparing the position of shear planes in the simulated videos (in the ESM) and the experimental atomic phase images under different loads, it was indicated that some individual fluorinated molecules can act as the lubricating molecules between the tip and the bulk self-assembled layer, as a result, the friction coefficient can be significantly reduced. The MD simulation results and experimental results are consistent with each other.

4 Conclusions

On the basis of the previously reported material synthesis and self-assembly methods, our work demonstrated that self-assembled fluorinated azobenzene layer achieved superlubricity under ultrahigh contact pressure, through the construction of a novel self-assembled fluorinated azobenzene layer on highly-oriented pyrolytic graphite (HOPG) substrate. The friction effect of the fluorinated molecular layer has reached the low friction under ultrahigh contact pressure obtained, which is significantly different from that reported in other two-dimensional material systems. Based on the molecular dynamics (MD) and density functional theory (DFT) simulation results, molecular fluorination increases effective and robust lubrication between the tip and the self-assembled layer, and leads to higher rigidity reducing the stress concentration in the substrate.

Our study elucidates that the outstanding microstructure of the self-assembled layer grown on the substrate changes friction behaviors to a low friction state under ultrahigh contact pressure in a positive manner. This work opens new approaches for further exploring the origins of friction and provides useful guidelines for the establishment of a better theoretical model on superlubricity to understand the rules on the regulation of friction properties at

the molecular level. Exploration of the mechanism regulating the friction state can provide a new approach to avoid the failure of ultralow friction coefficient under relatively high contact pressure, which has promising potential application in the future.

Acknowledgements

The authors would like to acknowledge the support of the National Natural Science Foundation of China (51922058).

Declaration of competing interest

The authors have no competing interests to declare that are relevant to the content of this article. The author Yu TIAN is the Editorial Board Member of this journal. The author Jianbin LUO is the Editor-in-Chief of this journal.

Electronic Supplementary Material: Supplementary material is available in the online version of this article at https://doi.org/10.1007/s40544-023-0782-2.

References

[1] Ma L R, Luo J B. Thin film lubrication in the past 20 years. *Friction* **4**(4): 280–302 (2016)

[2] Zhang Z, OuYang W, Liang X X, Yan X P, Yuan C Q, Zhou X C, Guo Z W, Dong C L, Liu Z L, Jin Y, Xiao J H. Review of the evolution and prevention of friction, wear, and noise for water-lubricated bearings used in ships. *Friction* **12**(1): 1–38 (2024)

[3] Han T Y, Zhang S W, Zhang C H. Unlocking the secrets behind liquid superlubricity: A state-ofthe-art review on phenomena and mechanisms. *Friction* **10**(8): 1137–1165 (2022)

[4] Yuan S H, Zhang C H. A sulfonated modification of PEEK for ultralow friction. *Friction* **11**(6): 881–893 (2023)

[5] Du C H, Yu T T, Wu Z S, Zhang L Q, Shen R L, Li X J, Feng M, Feng Y G, Wang D A. Achieving macroscale superlubricity with ultra-short running-in period by using polyethylene glycol-tannic acid complex green lubricant. *Friction* **11**(5): 748–762 (2023)

[6] Shinjo K, Hirano M. Dynamics of friction: Superlubric state. *Surf Sci* **283**: 473–478 (1993)

[7] Hirano M, Shinjo K. Atomistic locking and friction. *Phys Rev B* **41**: 11837–11851 (1990)

[8] Sokoloff J B. Theory of energy dissipation in sliding crystal surfaces. *Phys Rev B* **42**: 760–765 (1990)

[9] Bhushan B. Nanotribology and nanomechanics of MEMS/NEMS and BioMEMS/BioNEMS materials and devices. *Microelectron Eng* **84**: 387–412 (2007)

[10] Holmberg K, Erdemir A. Influence of tribology on global energy consumption, costs and emissions. *Friction* **5**(3): 263–284 (2017)

[11] Ren X Y, Yang X, Xie G X, He F, Wang R, Zhang C H, Guo D, Luo J B. Superlubricity under ultrahigh contact pressure enabled by partially oxidized black phosphorus nanosheets. *npj 2D Mater Appl* **5**: 44 (2021)

[12] Liu S W, Wang H P, Xu Q, Ma T B, Yu G, Zhang C, Geng D, Yu Z, Zhang S, Wang W, Hu Y Z, Wang H, Luo J B. Robust microscale superlubricity under high contact pressure enabled by graphene-coated microsphere. *Nat Commun* **8**: 14029 (2017)

[13] Li J J, Li J F, Luo J B. Superlubricity of graphite sliding against graphene nanoflake under ultrahigh contact pressure. *Adv Sci* **5**: 1800810 (2018)

[14] Maboudian R, Ashurst W R, Carraro C. Self-assembled monolayers as anti-stiction coatings for MEMS: characteristics and recent developments. *Sens Actuators A* **82**: 219–223 (2000)

[15] Srinivasan U, Houston M R, Howe R T, Maboudian R. Alkyltrichlorosilane-based self-assembled monolayer films for stiction reduction in silicon micromachines. *J Microelectromech Syst* **7**: 252–260 (1998)

[16] Wang D M, Chen G R, Li C K, Cheng M, Yang W, Wu S, Xie G B, Zhang J, Zhao J, Lu X B, et al. Thermally induced graphene rotation on hexagonal boron nitride. *Phys Rev Lett* **116**: 126101 (2016)

[17] Tan S C, Tao J Y, Luo W D, Shi H Y, Tu B, Jiang H, Liu Y H, Xu H J, Zeng Q D. Insight into the superlubricity and self-assembly of liquid crystals. *Front Chem* **9**: 668794 (2021)

[18] Li J J, Luo J B. Superlow friction of graphite induced by the self-assembly of sodium dodecyl sulfate molecular layers. *Langmuir* **33**: 12596–12601 (2017)

[19] Li J F, Cao W, Li J J, Ma M. Fluorination to enhance superlubricity performance between self-assembled monolayer and graphite in water. *J Colloid Interface Sci* **596**: 44–53 (2021)

[20] O' Hagan D. Understanding organofluorine chemistry: An introduction to the C–F bond. *Chem Soc Rev* **37**: 308–319 (2008)

[21] Lutfor M R, Hegde G, Kumar S, Tschierske C, Chigrinov V G. Synthesis and characterization of bent-shaped azobenzene monomers: Guest–host effects in liquid crystals with azo dyes for optical image storage devices. *Opt Mater* **32**: 176–183 (2009)

[22] Elinski M B, Menard B D, Liu Z, Batteas J D. Adhesion and friction at graphene/self-assembled monolayer interfaces investigated by atomic force microscopy. *J Phys Chem C* **121**: 5635–5641 (2017)

[23] Qian L M, Tian F, Xiao X D. Tribological properties of self-assembled monolayers and their substrates under various humid environments. *Tribol Lett* **15**: 169–176 (2003)

[24] Tsukruk V V, Bliznyuk V N. Adhesive and friction forces between chemically modified silicon and silicon nitride surfaces. *Langmuir* **14**: 446–455 (1998)

[25] Beharry A A, Woolley G A. Azobenzene photoswitches for biomolecules. *Chem Soc Rev* **40**: 4422–4437 (2011)

[26] Bandara H M, Burdette S C. Photoisomerization in different classes of azobenzene. *Chem Soc Rev* **41**: 1809–1825 (2012)

[27] Dokić J, Gothe M, Wirth J, Peters M V, Schwarz J, Hecht S, Saalfrank P. Quantum chemical investigation of thermal Cis-to-Trans isomerization of azobenzene derivatives: Substituent effects, solvent effects, and comparison to experimental data. *J Phys Chem A* **113**: 6763–6773 (2009)

[28] Hendrikx M, Schenning A P H J, Broer D J. Patterned oscillating topographical changes in photoresponsive polymer coatings. *Soft Matter* **13**: 4321–4327 (2017)

[29] Held P A, Gao H Y, Liu L, Mück-Lichtenfeld C, Timmer A, Moenig H, Barton D, Neugebauer J, Fuchs H, Studer A. On-surface domino reactions: Glaser coupling and dehydrogenative coupling of a biscarboxylic acid to form polymeric bisacylperoxides. *Angew Chem Int Ed* **55**: 9777–9782 (2016)

[30] Pauluth D, Tarumi K. Advanced liquid crystals for television. *J Mater Chem* **14**: 1219–1227 (2004)

[31] Dickey J B, Towne E B, Bloom M S, Taylor G J, Hill H M, Corbitt R A, McCall M A, Moore W H, Hedberg D G. Effect of fluorine substitution on color and fastness of monoazo dyes. *Ind Eng Chem* **45**: 1730–1734 (1953)

[32] Coelho P J, Castro M C R, Fonseca A M C, Raposo M M M. Photoswitching in azo dyes bearing thienylpyrrole and benzothiazole heterocyclic systems. *Dyes Pigm* **92**: 745–748 (2012)

[33] Wang S X, Wang, X. M.; Li, L. J.; Advincula, R. C. Design, synthesis, and photochemical behavior of poly (benzyl ester) dendrimers with azobenzene groups throughout their architecture. *J Org Chem* **69**: 9073–9084 (2004)

[34] Xue D D, Ma L R, Tian Y, Zeng Q D, Tu B, Luo W D, Wen S Z, Luo J B. Light-controlled friction by carboxylic azobenzene molecular self-assembly layers. *Front Chem* **9**: 707232 (2021)

[35] Liu P, Xue Q J, Tian J, Liu W M. Self-assembly of functional silanes onto silica nanoparticles. *Chin J Chem Phys* **16**: 481–486 (2003)

[36] Golub M A, Lopata E S, Finney L S. X-ray photoelectron spectroscopy study of the effect of hydrocarbon contamination on poly (tetrafluoroethylene) exposed to a nitrogen plasma. *Langmuir* **9**: 2240–2242 (1993)

[37] Sleigh C, Pijpers A P, Jaspers A, Coussens B, Meier R J. On the determination of atomic charge via ESCA including application to organometallics. *J Electron Spectrosc Relat Phenom* **77**: 41–57 (1996)

[38] Plimpton S. Fast parallel algorithms for short-range molecular-dynamics. *J Comput Phys* **117**: 1–19 (1995)

[39] Hutter J L, Bechhoefer J. Calibration of atomic-force microscope tips. *Rev Sci Instrum* **64**: 1868–1873 (1993)

[40] Varenberg M, Etsion I, Halperin G. An improved wedge calibration method for lateral force in atomic force microscopy. *Rev Sci Instrum* **74**: 3362–3367 (2003)

[41] Delley B. From molecules to solids with the DMol(3) approach. *J Chem Phys* **113**: 7756–7764 (2000)

[42] Perdew J P, Wang Y. Accurate and simple analytic representation of the electron-gas correlation energy. *Phys Rev B* **45**: 13244–13249 (1992)

[43] MacLeod J M, Lipton-Duffin J A, Cui D, De Feyter S, Rosei F. Substrate effects in the supramolecular assembly of 1,3,5-benzene tricarboxylic acid on graphite and graphene. *Langmuir* **31**: 7016–7024 (2015)

[44] Lindsay L, Broido D A. Optimized tersoff and brenner empirical potential parameters for lattice dynamics and phonon thermal transport in carbon nanotubes and graphene. *Phys Rev B* **81**: 205441 (2010)

[45] Qi Y Z, Liu J, Zhang J, Dong Y L, Li Q Y. Wear resistance limited by step edge failure: The rise and fall ofgraphene as an atomically thin lubricating material. *ACS Appl Mater Interfaces* **9**: 1099–1106 (2017)

[46] Jorgensen W L, Tirado-Rives J. Potential energy functions for atomic-level simulations of water and organic and biomolecular systems. *Proc Natl Acad Sci USA* **102**: 6665–6670 (2005)

[47] Toxvaerd S, Dyre J C. Communication: Shifted forces in molecular dynamics. *J Chem Phys* **134**: 081102 (2011)

[48] Bernardi S, Todd B D, Searles D J. Thermostating highly confined fluids. *J Chem Phys* **132**: 244706 (2010)

Dandan XUE. She is a Ph.D. candidate in the State Key Laboratory of Tribology in Advanced Equipment at Tsinghua University. Her current research interests include tribological behavior and mechanism of functionalized organic molecules.

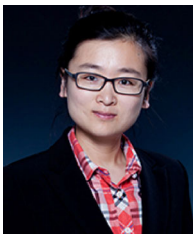

Liran MA. She received her B.S. degree from Tsinghua University in 2005, and received her Ph.D. degree from Tsinghua University in 2010. Following a postdoctoral period at the Weizmann Institute of Science in Israel, she is now working as an associate professor in the State Key Laboratory of Tribology in Advanced Equipment, Tsinghua University. Her interests in tribology have ranged from aqueous lubrication and hydration lubrication to the liquid/solid interface properties. She has published over 50 papers. Her honors include the Hinwin Doctoral Dissertation Award (2011), the Maple Leaf Award for Outstanding Young Tribologists (2015), and Chang Jiang Scholars Program-Young Professor Award (2015).

Yu TIAN. He is a professor and director of the State Key Laboratory of Tribology at Tsinghua University of China. He gained his B.S. and Ph.D. degrees in mechanical engineering at Tsinghua University in 1998 and 2002, respectively. Subsequently, he joined the State Key Laboratory of Tribology in Advanced Equipment. He was a postdoc at the University of California, Santa Barbara with professor Jacob ISRAELACHVILI from 2005 to 2007. His research interest is the science and technology at the interface of physics, materials, engineering, and biology to understand the physical laws of adhesion, friction, and rheology to implement technological inventions to benefit the society. He has published over 150 peer-reviewed journal papers. He has received the Youth Science and Technology Award of China (2016), the Yangtze River Scholars Distinguished Professor (2015–2019), the National Natural Science Foundation for Distinguished Young Scientists of China (2014), the Wen Shizhu-Maple Award-Young Scholar Award (2012), the Young Scholar Achievement Award of the Society of Mechanical Engineering of China (2011), Outstanding Young Scholar Award of the Chinese Tribology Institute (2009), and the National Excellent Doctoral Dissertation of China (2004).

Ming MA. He received his Ph.D. degree in engineering mechanics from Tsinghua University, China, in 2011. He joined the State Key Laboratory of Tribology in Advanced Equipment at Tsinghua University since 2016. His current position is an associate professor. His research areas cover nano-tribology, nanofluidics, superlubricity, and diffusion on surfaces or under confinement.

Qingdao ZENG. He is a professor at the National Center for Nanoscience and Technology, China. He received his Ph.D. degree in inorganic chemistry from Nanjing University, China, in 1997. After this, he worked as a postdoctoral researcher (1997–2000) and an associate professor (2000–2007) at the Institute of Chemistry, Chinese Academy of Sciences, China. He is the author or coauthor of more than 300 original papers in peer reviewed international journals, including *J. Am. Chem. Soc.*, *Angew. Chem., Int. Ed.*, *Nano Lett.*, and *ACS Nano*, etc. His current research interest focuses on the construction of molecular nanostructures and the fabrication of nanostructures based on organic molecules.